

PAPER • OPEN ACCESS

Application of a meshless space-time adaptive approach to phase-field modelling of polycrystalline solidification

To cite this article: T Dobravec *et al* 2023 *IOP Conf. Ser.: Mater. Sci. Eng.* **1281** 012057

View the [article online](#) for updates and enhancements.

You may also like

- [Phase field modelling of dendritic solidification by using an adaptive meshless solution procedure](#)
T Dobravec, B Mavri and B Šarler
- [A meshless quasicontinuum method based on local maximum-entropy interpolation](#)
Dennis M Kochmann and Gabriela N Venturini
- [A robust numerical approximation of advection diffusion equations with nonsingular kernel derivative](#)
Kamran, Ali Ahmadian, Soheil Salahshour et al.

PRIME
PACIFIC RIM MEETING
ON ELECTROCHEMICAL
AND SOLID STATE SCIENCE

HONOLULU, HI
Oct 6–11, 2024

Abstract submission deadline:
April 12, 2024

Learn more and submit!

Joint Meeting of
The Electrochemical Society
•
The Electrochemical Society of Japan
•
Korea Electrochemical Society

Application of a meshless space-time adaptive approach to phase-field modelling of polycrystalline solidification

T Dobravec¹, B Mavrič^{1,2} and B Šarler^{1,3}

¹ Faculty of Mechanical Engineering, University of Ljubljana, Aškerčeva cesta 6, Ljubljana, SI-1000, Slovenia

² Division of Scientific Computing, Department of Information Technology, Uppsala University, P.O. Box 337, Uppsala, SE-751 05, Sweden

³ Institute of Metals and Technology, Lepi pot 11, Ljubljana, SI-1000, Slovenia

E-mail: tadej.dobravec@fs.uni-lj.si

Abstract. We have developed a 2-D numerical meshless adaptive approach for phase-field modelling of dendritic solidification. The quadtree-based approach decomposes the computational domain into quadtree sub-domains of different sizes. The algorithm generates uniformly-distributed computational nodes in each quadtree sub-domain. We apply the meshless radial basis function generated finite difference method and the forward Euler scheme to discretise governing equations in each computational node. The fixed ratio between the characteristic size and the node spacing of a quadtree sub-domain ensures space adaptivity. The adaptive time-stepping accelerates the calculations further. In the framework of previous research studies, we used the approach to solve quantitative phase-field models for single dendrite growth in pure melts and dilute binary alloys. In the present study, we upgrade the solution procedure for the modelling growth of multiple differently oriented dendrites. Along with the space-time adaptive approach, we apply non-linear preconditioning of the phase-field equation to increase computational efficiency. We investigate a novel numerical approach's accuracy and computational efficiency by simulating the equiaxed dendrite growth from a dilute binary alloy.

1. Introduction

Numerical modelling of dendritic solidification represents an important task for predicting the microstructure evolution of many metals at different casting conditions [1,2]. The microstructure evolution is closely linked to the material properties of the solidified material. The numerical models are, therefore, crucial for the design and production of high-quality castings. In the present study, we employ the phase-field (PF) method for modelling dendritic solidification. The PF method [3,4] represents a powerful tool for solving many free boundary problems in material science and engineering [5].

In the previous studies, we consider PF models for simulating single dendrite growth in pure melts and dilute binary alloys [6,7]. In this paper, we extend the test case for the single dendrite solidification of dilute binary alloys [8] to polycrystalline solidification. There are two main PF approaches for modelling this situation, which is important for the practice. The first approach is the multi-PF model [9–11], where each of the grains is represented by its own PF. This



approach provides a detailed framework for analysing grain boundary evolution. However, multi-PF simulations experience significant memory usage and long computational times. The second approach is the orientation field method [12–15]. This approach complements the PF model with information on the grain orientation. As a result, the related orientation field method is computationally much less demanding and can be used for PF modelling of many simultaneously growing dendrites [16]. The latter approach, however, experiences a limitation, i.e., the standard governing equation for the orientation field is incorrect in coherent polycrystalline matter [17]. In this paper, we consider early-stage equiaxed solidification of dilute binary alloys. In this case, the orientation field method does not experience the mentioned limitation [17]. Our primary focus is the solidification of multiple differently-oriented dendrites before the impingement. Therefore, we do not have to account for the physics of grain boundaries. For this purpose, the front-tracking (FT) algorithm [18] represents a very suitable and computationally efficient algorithm for tracking the preferential growth direction of each dendrite. Additionally, we employ the non-linear preconditioning of the PF equation to increase computational efficiency [19–21].

Researchers developed many different computational approaches for the PF modelling of dendritic growth in the last 20 years, e.g., adaptive mesh refinement [22], parallel simulations using graphic processing units [23], implicit time-stepping and multi-grid approaches [24], etc. In this paper, we employ the space-time adaptive algorithm to accelerate the meshless PF modelling of dendritic solidification [7]. Meshless methods represent a fast-growing family of numerical methods that do not rely on the division in space in elements like finite element or finite volume methods. The representatives of this family are the element-free Galerkin method [25], the smoothed particle hydrodynamics method [26], the meshless-collocation method [27], etc. In the present study, we employ the local radial basis function collocation method (LRBFCM) [28], also known as the radial basis function generated finite difference (RBF-FD) method [29]. The meshless RBF-FD method is especially suitable for orientation-insensitive PF modelling of dendritic solidification in arbitrary preferential growth directions [6].

2. Governing equations

We consider the isothermal solidification of a dilute supersaturated binary alloy in the 2-D computational domain Ω with the boundary Γ . A simplified case is studied where the solute diffusivity in the liquid phase D_ℓ , the chemical capillary length d_c , and the partition coefficient k_0 are constant. The solute diffusion in the solid phase is neglected. We define supersaturation U as

$$U = \frac{C_\ell - C_\ell^e}{(1 - k_0)C_\ell^e}, \quad (1)$$

where C_ℓ and C_ℓ^e stand for the solute concentration in the liquid phase and the equilibrium solute concentration in the liquid phase, defined from the phase diagram, respectively. We use the dimensionless PF model [8], where the spatial and temporal coordinates are measured in units of the PF interface thickness and the PF characteristic attachment time, respectively. The PF interface thickness is defined as

$$W_0 = d_c \frac{1}{\alpha_1} \lambda, \quad (2)$$

where α_1 stands for a constant and λ for the free parameter of the PF model. The PF characteristic attachment time is given as

$$\tau_0 = \frac{d_c^2}{D_\ell} \frac{\alpha_2}{\alpha_1^2} \lambda^3, \quad (3)$$

where α_2 stands for a constant of the PF model. The PF constants are equal to $\alpha_1 = 0.8839$ and $\alpha_2 = 0.6267$ [30]. The selection of free parameter λ has to yield W_0 much smaller than the

diffusion length of solidification to ensure a valid PF model. The PF model [8] constrains the PF ϕ in the interval $-1 \leq \phi \leq 1$, where $\phi = 1$ and $\phi = -1$ denote solid and liquid phases, respectively. We use the preconditioned PF variable ψ , defined as [19]

$$\psi = \sqrt{2} \tanh^{-1}(\phi), \quad (4)$$

to increase numerical stability for larger node spacings.

2.1. Equations for ψ and U

The governing equation for ψ reads [20]

$$a^2(\mathbf{n}) \frac{\partial \psi}{\partial t} = \sqrt{2} (\phi - \lambda(1 - \phi)U) + 2a(\mathbf{n}) \nabla a(\mathbf{n}) \cdot \nabla \psi - \sqrt{2} \phi \nabla \psi \cdot \mathbf{a}(\mathbf{n}) + \nabla \cdot \mathbf{a}(\mathbf{n}) + a^2(\mathbf{n}) \left(\nabla^2 \psi - \sqrt{2} \phi |\nabla \psi|^2 \right), \quad (5)$$

where $a(\mathbf{n})$ and $\mathbf{a}(\mathbf{n})$ stand for the anisotropy function and vector, respectively. They depend on the solid-liquid interface normal

$$\mathbf{n} = -\frac{\nabla \psi}{|\nabla \psi|}, \quad (6)$$

and are defined in the following subsection. The governing equation for U reads as

$$\begin{aligned} \frac{1}{2} (1 + k_0 - (1 - k_0) \phi) \frac{\partial U}{\partial t} &= D \frac{1 - \phi}{2} \nabla^2 U - D \frac{1 - \phi^2}{2\sqrt{2}} \nabla U \cdot \nabla \psi \\ &- \frac{1}{2\sqrt{2}} ((1 + (1 - k_0)U) \nabla G \cdot \mathbf{n} + G(1 - k_0) \nabla U \cdot \mathbf{n}) \\ &- \frac{G}{2} \left[1 + (1 - k_0)U \left(1 - \frac{\nabla \cdot \mathbf{n}}{\sqrt{2}} \right) \right], \end{aligned} \quad (7)$$

where $D = D_\ell \tau_0 / W_0^2$ is the dimensionless solute diffusivity in the liquid phase, and the scalar G is defined as

$$G = \frac{1 - \phi^2}{\sqrt{2}} \frac{\partial \psi}{\partial t}. \quad (8)$$

2.2. Anisotropy of the surface energy

Let's denote the anisotropy function and vector in a dendrite's coordinate system as $\tilde{a}(\mathbf{m})$ and $\tilde{\mathbf{a}}(\mathbf{m})$, where $\mathbf{m} = (m_x, m_y)$ represents the normal to the interface in a dendrite's coordinate system. We employ the cubic anisotropy function

$$\tilde{a}(\mathbf{m}) = 1 - 3\epsilon_4 + 4\epsilon_4 (m_x^4 + m_y^4), \quad (9)$$

where ϵ_4 stands for the anisotropy strength of the interface energy. Function $\tilde{a}(\mathbf{m})$ yields anisotropy vector [20]

$$\tilde{\mathbf{a}}(\mathbf{m}) = 16\epsilon_4 |\nabla \psi| \tilde{a}(\mathbf{m}) [m_x(m_x^4 + m_y^4 - m_x^2), m_y(m_x^4 + m_y^4 - m_y^2)]. \quad (10)$$

Function $a(\mathbf{n})$ from equation (5) is obtained with the following relation

$$a(\mathbf{n}) = \tilde{a}(\mathbf{R}^T \mathbf{n}), \quad \mathbf{R} = \begin{bmatrix} \cos(\theta) & -\sin(\theta) \\ \sin(\theta) & \cos(\theta) \end{bmatrix}, \quad (11)$$

where \mathbf{R} is the rotation matrix and θ stands for the preferential growth direction angle. We employ the following relation to obtain $\mathbf{a}(\mathbf{n})$ from equation (5)

$$\mathbf{a}(\mathbf{n}) = \mathbf{R} \tilde{\mathbf{a}}(\mathbf{R}^T \mathbf{n}). \quad (12)$$

3. Solution procedure

3.1. Solution of governing equations for ψ and U

We solve the governing equations for ψ and U by our previously developed space-time adaptive approach [7]. It is based on dynamic quadtree domain decomposition, as seen in figure 1. Regular or scattered node distribution with fixed node spacing is generated in each quadtree sub-domain; in the present study, we employ regular node distribution. The constant ratio m_Ω between a quadtree sub-domain's side length and node spacing ensures space adaptivity, as seen on the left in figure 1. The free parameters of the space-time adaptive approach are the minimum spacing h , the ratio m_Ω , the maximum number of different node spacings n_h , the maximum number of different time steps $n_{\Delta t}$, and the overlapping parameter $n_{overlap}$ [7]. In this paper, we set $n_{overlap} = 1$ and $n_{\Delta t} = 2$; such configuration yields good accuracy and computational efficiency [7]. In subsection 4.1, we analyse the influence of minimum spacing h on the accuracy.

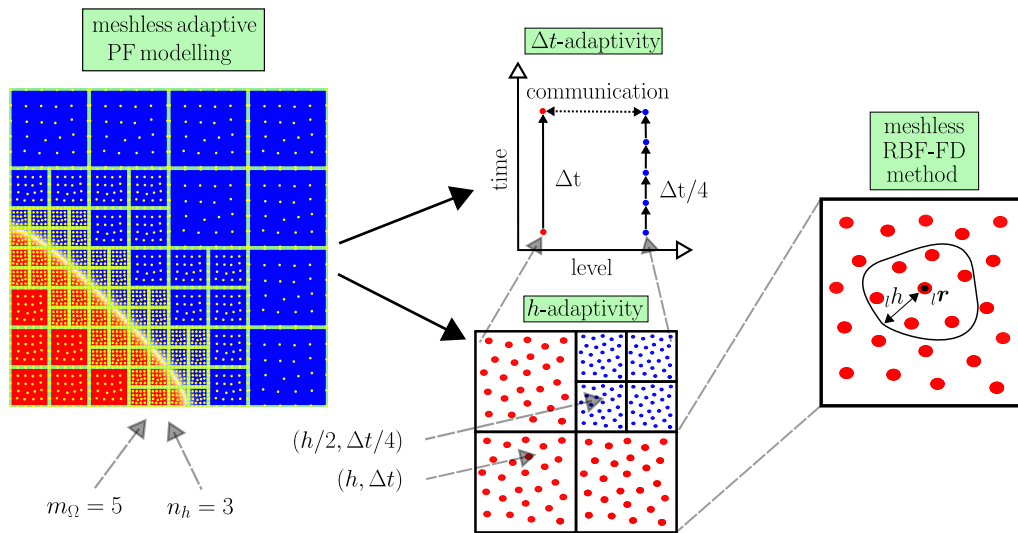


Figure 1. A scheme of space-time adaptive meshless solution procedure. The quadtree-based approach ensures a high density of computational nodes and fine time-stepping at and near the solid-liquid interface. The solution procedure employs the meshless RBF-FD method for spatial discretisation of equations for ψ and U in each quadtree sub-domain.

We apply the forward Euler scheme and the meshless RBF-FD method to discretise the governing equations for ψ and U in the computational nodes from a quadtree sub-domain. We calculate the minimum stable time step in the forward Euler scheme as

$$\Delta t = \alpha_{\Delta t} \frac{1}{4} \frac{h^2}{\max(D, 1/(1 - \epsilon_4))}, \quad (13)$$

where $\alpha_{\Delta t}$ stands for the time step stability parameter. Value $\alpha_{\Delta t} = 0.2$ yields sufficiently small time steps for solving the considered PF model, i.e., further refinement of $\alpha_{\Delta t}$ has a negligible effect on accuracy. We employ adaptive time-stepping to increase computational efficiency. The stable time step depends on node spacing; hence, larger time steps can be used in quadtree sub-domains with larger node spacing, as seen in figure 1. We employ fifth-degree polyharmonic splines as radial basis functions, second-order augmentation with monomials, and thirteen nodes in a local support domain in the meshless RBF-FD method. We have previously shown that such a configuration is very suitable out of many tested configurations for the PF modelling of dendritic growth [6, 7].

A PF model can be accurately resolved using larger node spacings when employing preconditioning [19–21]. However, when we use space adaptivity, the preconditioning yields stability issues far from the solid-liquid interface, where very large node spacings can not resolve the model. Solving a non-preconditioned PF model by space adaptive algorithm does not experience this problem since the PF is a constant far away from the solid-liquid interface. We tackle this problem by applying the following restriction [16]

$$\psi = \begin{cases} \psi_c & \psi > \psi_c \\ -\psi_c & \psi < -\psi_c \\ \psi & -\psi_c \leq \psi \leq \psi_c \end{cases}, \quad (14)$$

where ψ_c is the numerical cut-off parameter. The adaptive algorithm ensures the minimum node spacing h where $|\psi| < \psi_c - 1.0$. Regions where $|\psi| > \psi_c - 0.5$ can be de-refined. Care is taken to keep the quadtree balanced in the refinement/de-refinement procedure. Details of the space-time adaptive algorithm can be found in [7]. In subsection 4.1, we analyse the influence of parameter ψ_c on the accuracy.

3.2. Front-tracking of the grain orientation

We use the FT algorithm [18] to track the preferential growth direction angle of each dendrite in Ω . Along with $\psi(\mathbf{r})$ and $U(\mathbf{r})$, we also define position-dependent orientation field $\theta(\mathbf{r})$, which is used for calculating $a(\mathbf{n})$ and $\mathbf{a}(\mathbf{n})$ in equations (11) and (12). When we consider single dendrite growth or multiple dendrite growth with the same preferential growth direction θ_0 , $\theta(\mathbf{r}) = \theta_0$ throughout simulation.

Suppose a particle with a radius r_0 , centre \mathbf{r}_0 , and orientation angle $\theta_0 \in (0, \pi/2]$ nucleates in Ω . The initial condition for ψ reads as

$$\psi(\mathbf{r}, t = 0) = r_0 - |\mathbf{r} - \mathbf{r}_0|. \quad (15)$$

We define the initial condition for θ as

$$\theta(\mathbf{r}, t = 0) = \begin{cases} \theta_0 & |r_0 - |\mathbf{r} - \mathbf{r}_0|| \leq \psi_{FT} \\ 0 & |r_0 - |\mathbf{r} - \mathbf{r}_0|| > \psi_{FT} \end{cases}, \quad (16)$$

where ψ_{FT} is the FT thickness of the boundary layer around the solid-liquid interface. Value $\theta = 0$ represents the bulk of the solid or liquid phase, while values $\theta > 0$ represent the FT boundary layer surrounding the solid-liquid interface.

As ψ evolves, the FT algorithm applies in a computational node $\mathbf{r}_i \in \Omega$ to track the orientation of a growing dendrite. Suppose $\{\mathbf{r}_j\}_{\mathbf{r}_i}$ is a set of nodes nearest to \mathbf{r}_i . The FT algorithm sets the orientation field as

$$\theta(\mathbf{r}_i, t) = \begin{cases} 0 & |\psi(\mathbf{r}_i, t)| > \psi_{FT} \\ \theta(\mathbf{r}_i, t) & \theta(\mathbf{r}_i, t) > 0 \\ \theta(\mathbf{r}_j, t) & \theta(\mathbf{r}_i, t) = 0 \end{cases}, \quad (17)$$

where $\theta(\mathbf{r}_j, t) > 0$ and $|\psi(\mathbf{r}_j, t)| \leq \psi_{FT}$ for $\mathbf{r}_j \in \{\mathbf{r}_j\}_{\mathbf{r}_i}$. The algorithm performs a loop over a set of nearest nodes $\{\mathbf{r}_j\}_{\mathbf{r}_i}$ when checking the last condition from equation (17). When conditions $\theta(\mathbf{r}_j, t) > 0$ and $|\psi(\mathbf{r}_j, t)| \leq \psi_{FT}$ are fulfilled for $\mathbf{r}_j \in \{\mathbf{r}_j\}_{\mathbf{r}_i}$, the algorithm sets $\theta(\mathbf{r}_i, t) = \theta(\mathbf{r}_j, t)$, exits the loop over $\mathbf{r}_j \in \{\mathbf{r}_j\}_{\mathbf{r}_i}$, and moves to the next computational node $\mathbf{r}_i \in \Omega$. In subsection 4.1, we analyse the influence of parameter ψ_{FT} to the accuracy.

4. Results

We verify the present numerical model by solving the test case for a single dendrite growth [8]. The influence of the free parameters on the accuracy of modelling growth in arbitrary growth directions is investigated. Next, we extend the test case for a single dendrite growth [8] to the solidification of multiple randomly-oriented dendrites.

4.1. Verification of the numerical model

The test case [8] considers the growth of a single dendrite from a supersaturated dilute binary alloy in a square computational domain $\Omega = [-L/2, L/2] \times [-L/2, L/2]$, where L stands for the size of the computational domain. We set the initial condition for ψ according to equation (15). The initial condition for U reads as $U(\mathbf{r}, t = 0) = -\Delta$, where Δ stands for the initial supersaturation. Zero flux Neumann boundary conditions are applied for ψ and U

$$\nabla\psi\Big|_{\Gamma} \cdot \mathbf{n}_{\Gamma} = 0, \quad \nabla U\Big|_{\Gamma} \cdot \mathbf{n}_{\Gamma} = 0, \quad (18)$$

where \mathbf{n}_{Γ} is the outward-facing normal to Γ . Table 1 contains the simulation parameters used in verification of our numerical model.

Table 1. Simulation parameters for verifying the numerical model.

<i>Computational domain</i>	
Size of domain (L)	537.6
<i>Physical problem</i>	
Strength of anisotropy (ϵ_4)	0.02
Initial supersaturation (Δ)	0.55
Center of nucleus (\mathbf{r}_0)	(0, 0)
Radius of nucleus (r_0)	$22\alpha_1\alpha_2/2$
Partition coefficient (k_0)	0.15
<i>PF model</i>	
Constant (α_1)	0.8839
Constant (α_2)	0.6267
Coupling parameter (λ)	$2/\alpha_2$
Dimensionless solute diffusivity (D)	2

We analyse first the influence of the minimum node spacing h on the accuracy. In this analysis, the orientation field is constant in the whole Ω , i.e., we turn off the FT algorithm and set $\theta(\mathbf{r}) = \theta_0$. The reason for the turned-off FT algorithm is to analyse only the influence of spacing h on the accuracy. We test the performance for the minimum node spacings $h = 0.4$, $h = 0.8$, $h = 1.2$, and $h = 1.4$. The following sets of free parameters are used ($n_h = 6, m_{\Omega} = 21$), ($n_h = 5, m_{\Omega} = 21$), ($n_h = 5, m_{\Omega} = 14$), and ($n_h = 5, m_{\Omega} = 12$) for $h = 0.4$, $h = 0.8$, $h = 1.2$, and $h = 1.4$, respectively. We set the numerical cut-off parameter to $\psi_c = 12$. Figure 2 shows the dendrite growth velocity as a function of time at $\theta_0 = 0$ for $h = 0.4$. The figure also shows Karma's reference solution [8], obtained using the finite-difference method with the node spacing $h = 0.4$ and the forward Euler scheme with the time step $\Delta t = 0.008$. We can see that our velocity agrees well with the reference solution. Figure 3 shows the steady-state dendrite growth velocity as a function angle θ_0 for four node spacings h . The steady-state velocity for $h = 0.4$ and $h = 0.8$ is approximately 1.9% above the reference solution and almost independent of θ_0 ,

while $h = 1.2$ and $h = 1.4$ yield θ_0 -dependent results. There are three main reasons for minor discrepancy with the reference solution at $h = 0.4$ and $h = 0.8$. First, contrary to [8], we employ preconditioned PF model. Second, we use different numerical methods to solve the PF model. And third, our algorithm for calculating growth velocity is probably not the same as in [8]. The steady-state velocity for $h = 1.2$ is closer to the reference solution. The difference between the maximum and the minimum velocity at $h = 1.2$ is approximately 1.6%. Nevertheless, we believe that $h = 1.2$ ensures high enough accuracy and is used for calculations in the rest of the paper. The value $h = 1.4$ is unsuitable for calculating this test case.

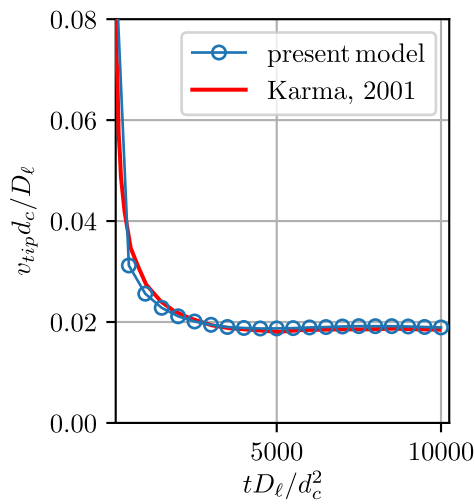


Figure 2. Dendrite growth velocity as a function of time.

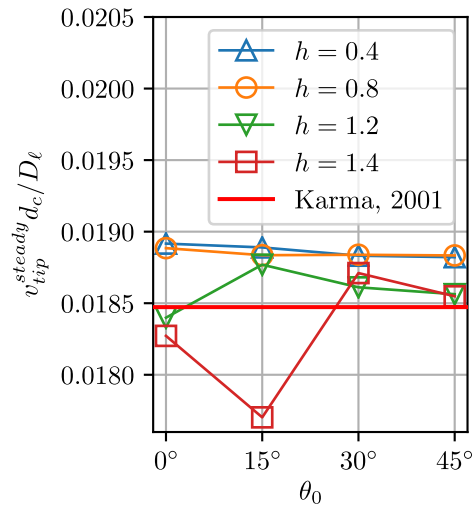


Figure 3. Steady-state dendrite growth velocity as a function of preferential growth direction angle θ_0 at four values of the node spacing h .

We next analyse the influence of the numerical cut-off parameter ψ_c on the accuracy. The FT algorithm is still turned off in this analysis. The reason for the turned-off FT algorithm is to analyse only the influence of parameter ψ_c on the accuracy. Figure 4 shows the steady-state dendrite growth velocity as a function angle θ_0 for five parameters ψ_c . Too small values of ψ_c significantly decrease the accuracy. The accuracy is no longer increased for $\psi_c \geq 12$. Therefore, we employ $\psi_c = 12$ for calculations in the rest of the paper. Finally, we turn on the FT algorithm and analyse the influence of the FT interface thickness ψ_{FT} to the accuracy. We set the initial condition for θ according to equation (16). Figure 5 shows the steady-state dendrite growth velocity as a function angle θ_0 for four parameters ψ_{FT} . As for parameter ψ_c , too small values of ψ_{FT} significantly decrease the accuracy. The accuracy is no longer increased for $\psi_{FT} \geq 5$. Therefore, we employ $\psi_{FT} = 5$ for calculations in the rest of the paper. To conclude, parameters $h = 1.2$, $\psi_c = 12$, and $\psi_{FT} = 5$ represent a good compromise between the accuracy and computational efficiency for the PF modelling of dendritic growth in arbitrary growth directions. We use this selection of parameters to simulate polycrystalline solidification in the following subsection.

4.2. Polycrystalline solidification

In this subsection, we extend the test case from the previous subsection to the growth of multiple randomly-oriented dendrites. We use the simulation parameters from table 1 with two differences. First, the size of Ω is set to $L = 1075.2$. And second, we have multiple centres

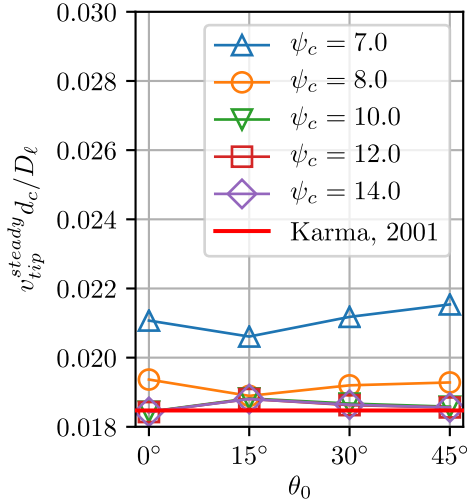


Figure 4. Steady-state dendrite growth velocity as a function of preferential growth direction angle θ_0 at five values of the cut-off parameter ψ_c .

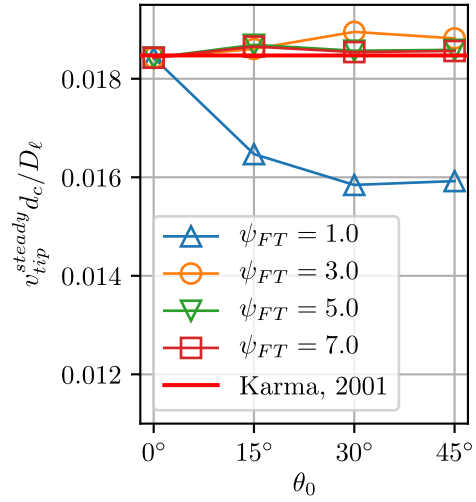


Figure 5. Steady-state dendrite growth velocity as a function of preferential growth direction angle θ_0 at four values of the orientation parameter ψ_{FT} .

of nuclei since we consider polycrystalline solidification. We use the same boundary condition for ψ and U as in the previous subsection. The initial condition for U is also the same. However, the initial conditions for ψ and θ have to be modified to describe the nucleation of multiple dendrites.

Nuclei are quasi-randomly positioned in Ω . For instance, if the number of nuclei is 4, we first divide a square Ω into 4 square sub-domains $\tilde{\Omega}$ of equal size. Suppose $\tilde{\mathbf{r}}_\Omega$ is the centre of $\tilde{\Omega}$. The quasi-random position of the nucleus $\mathbf{r}_0 \in \tilde{\Omega}$ is set as

$$\mathbf{r}_0 = \tilde{\mathbf{r}}_\Omega + 0.2\tilde{L}(\mathcal{R}_x, \mathcal{R}_y), \quad (19)$$

where \tilde{L} is the side length of $\tilde{\Omega}$ while $\mathcal{R}_x \in [-1, 1]$ and $\mathcal{R}_y \in [-1, 1]$ represent random numbers. The random orientation angle is similarly set as $\theta_0 = \pi/2\mathcal{R}_\theta$, where $\mathcal{R}_\theta \in (0, 1]$ is a random number. After we determine the sets of positions $\{\mathbf{r}_0\}$ and corresponding orientations $\{\theta_0\}$, we use the following equation for the initial condition for ψ

$$\psi(\mathbf{r}, t = 0) = \max_{\mathbf{r}'_0 \in \{\mathbf{r}_0\}} (r_0 - |\mathbf{r} - \mathbf{r}'_0|). \quad (20)$$

The initial condition for θ is set as $\theta(\mathbf{r}, t = 0) = \theta'_0$ if $|\mathbf{r}_0 - |\mathbf{r} - \mathbf{r}'_0|| \leq \psi_{FT}$ where \mathbf{r}'_0 and θ'_0 belong to the same nucleus. This condition is checked for all $\mathbf{r}'_0 \in \{\mathbf{r}_0\}$ and $\theta'_0 \in \{\theta_0\}$. The initial condition for θ is set as $\theta(\mathbf{r}, t = 0) = 0$ if $|\mathbf{r}_0 - |\mathbf{r} - \mathbf{r}'_0|| > \psi_{FT}$ for all $\mathbf{r}'_0 \in \{\mathbf{r}_0\}$.

Figure 6 shows rescaled concentration field C/C_ℓ^e in Ω in the case of four (top row), nine (middle row), and sixteen (bottom row) randomly oriented and quasi-randomly-positioned growing dendrites. In the first stage of solidification, dendrites freely grow into the melt. Their growth is constrained after they approach neighbouring dendrites. In the final stage, the dendrites become coarser and coarser. Naturally, the average dendrite's size and primary trunk thickness decrease as the number of nuclei increases.

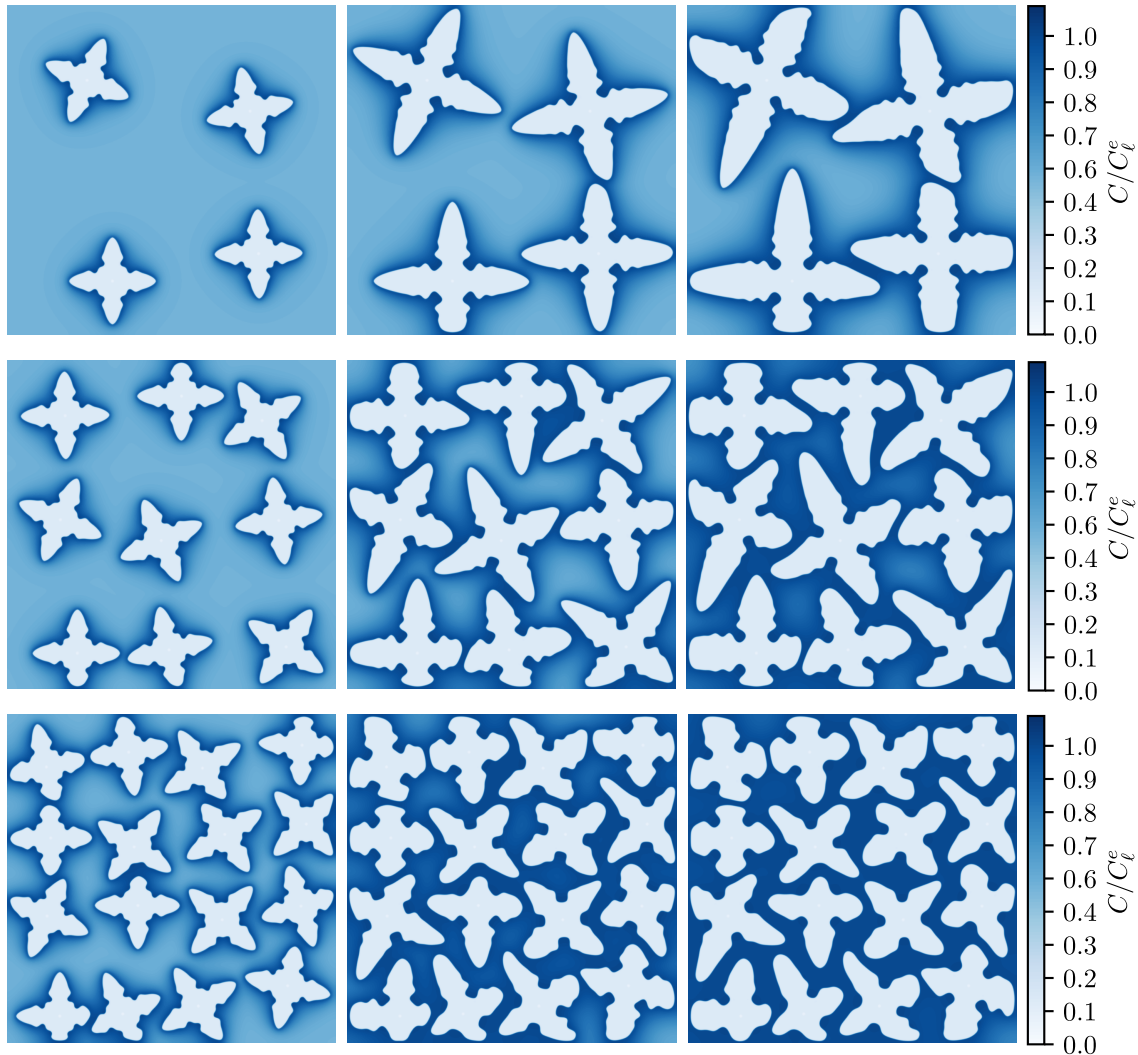


Figure 6. Rescaled concentration field C/C_ℓ^e in computational domain $\Omega = [-537.6, 537.6] \times [-537.6, 537.6]$ in the case of four (top row), nine (middle row), and sixteen (bottom row) randomly oriented and quasi-randomly-positioned growing dendrites. The field is plotted at $t = 1000$ (left column), $t = 2000$ (middle column), and $t = 3000$ (right column).

5. Conclusions

This paper demonstrates the use of meshless-based space-time adaptive numerical approach for the PF modelling of polycrystalline early-stage isothermal solidification of supersaturated dilute binary alloys. The approach, developed initially for modelling single dendrite growth, is extended to model the growth of multiple differently-oriented dendrites. We analyse the influence of the minimum node spacing h , the numerical cut-off parameter ψ_c , and the FT interface thickness ψ_{FT} to the accuracy in the case of single dendrite growth at different preferential growth directions. We show that the selection of parameters $h = 1.2$, $\psi_c = 12$, and $\psi_{FT} = 5$ represents the best compromise between accuracy and computational efficiency. We then simulate polycrystalline solidification in the case of four, nine, and sixteen randomly-oriented nuclei and obtain expected results.

The present paper shows that our numerical approach is suitable for the PF modelling of dendritic solidification. The approach can be easily extended to model the solidification of pure

melts and multi-component alloys. In the case of dilute binary and multi-component alloys, the model can be easily extended to simulate non-isothermal solidification in the frozen-temperature approximation, i.e., when the temperature is considered as an input parameter. In the future, the numerical approach will be extended to 3-D using an octree instead of a quadtree algorithm.

Acknowledgments

This work was supported by the Slovenian Research Agency as post-doctoral basic project Z2-4479, programme group P2-0162, and applied project L2-3173, also supported by Štore Steel company.

References

- [1] Kurz W, Fisher D J and Trivedi R 2019 *Int. Mater. Rev.* **64** 311–354
- [2] Kurz W, Rappaz M and Trivedi R 2021 *Int. Mater. Rev.* **66** 30–76
- [3] Chen L Q 2002 *Annu. Rev. Mater. Res.* **32** 113–140
- [4] Boettinger W J, Warren J A, Beckermann C and Karma A 2002 *Annu. Rev. Mater. Res.* **32** 163–194
- [5] Steinbach I 2009 *Model. Simul. Mat. Sci. Eng.* **17** 073001
- [6] Dobravec T, Mavrič B and Šarler B 2020 *Comput. Mater. Sci.* **172** 109166
- [7] Dobravec T, Mavrič B and Šarler B 2022 *Comput. Math. Appl.* **126** 77–99
- [8] Karma A 2001 *Phys. Rev. Lett.* **87** 115701
- [9] Steinbach I, Pezzolla F, Nestler B, Seeßelberg M, Prieler R, Schmitz G J and Rezende J L L 1996 *Phys. D: Nonlinear Phenom.* **94** 135–147
- [10] Moelans N, Blanpain B and Wollants P 2008 *Phys. Rev. B* **78** 024113
- [11] Ofori-Opoku N and Provatas N 2010 *Acta Mater.* **58** 2155–2164
- [12] Kobayashi R, Warren J A and Craig Carter W 2000 *Phys. D: Nonlinear Phenom.* **140** 141–150
- [13] Warren J A, Kobayashi R, Lobkovsky A E and Craig Carter W 2003 *Acta Mater.* **51** 6035–6058
- [14] Granasy L, Pusztai T and Warren J A 2004 *J. Phys. Condens. Matter* **16**
- [15] Pusztai T, Bortel G and Gránásy L 2005 *EPL* **71** 131
- [16] Gong T Z, Chen Y, Cao Y F, Kang X H and Li D Z 2018 *Comput. Mater. Sci.* **147** 338–352
- [17] Plapp M 2011 *Philos. Mag.* **91** 25–44
- [18] Chen Y, Qi X B, Li D Z, Kang X H and Xiao N M 2015 *Comput. Mater. Sci.* **104** 155–161
- [19] Glasner K 2001 *J. Comput. Phys.* **174** 695–711
- [20] Boukellal A K, Rouby M and Debierre J M 2021 *Comput. Mater. Sci.* **186** 110051
- [21] Tourret D and Karma A 2015 *Acta Mater.* **82** 64–83
- [22] Provatas N, Goldenfeld N and Dantzig J 1998 *Phys. Rev. Lett.* **80** 3308–3311
- [23] Takaki T, Shimokawabe T, Ohno M, Yamanaka A and Aoki T 2013 *J. Cryst. Growth* **382** 21–25
- [24] Bollada P C, Goodyer C E, Jimack P K, Mullis A M and Yang F W 2015 *J. Comput. Phys.* **287** 130–150
- [25] Belytschko T, Lu Y Y and Gu L 1994 *J. Numer. Methods Eng.* **37** 229–256
- [26] Liu G R and Liu M B 2003 *Smoothed Particle Hydrodynamics: A Meshfree Particle Method* (Singapore: World Scientific)
- [27] Kansa E J 1990 *Comput. Math. with Appl.* **19** 127–145
- [28] Šarler B and Vertnik R 2006 *Comput. Math. with Appl.* **51** 1269–1282
- [29] Flyer N, Fornberg B, Bayona V and Barnett G A 2016 *J. Comput. Phys.* **321** 21–38
- [30] Karma A and Rappel W J 1998 *Phys. Rev. E* **57** 4323